Probing cytoplasmic viscosity in the confined geometry of tip-growing plant cells via FRAP

James L. Kingsley,[†],[*] Jeffrey P. Bibeau, [‡],[*] Zhilu Chen[+], Xinming Huang[+], Luis Vidali,[‡],[**] Erkan Tüzel[†],[**]

[†]*Department of Physics, Worcester Polytechnic Institute, Worcester, MA, 01609, USA*
[‡]*Department of Biology and Biotechnology, Worcester Polytechnic Institute, Worcester, MA, 01609, USA*
[+]*Department of Electrical and Computer Engineering, Worcester Polytechnic Institute, Worcester, MA, 01609, USA*
[*] *co-first authors*
[**] *co-corresponding authors*

Abstract

Understanding plant growth and development is essential to develop the future technologies necessary to meet the anticipated needs of a growing world population. Because plant growth is a manifestation of cellular growth, it is of prime importance to develop a mechanistic understanding of plant cell growth. Transport of cellular cargo, such as proteins, in growing plant cells is essential as it facilitates growth. Developing a quantitative model of growth requires knowledge of the surrounding medium, i.e. the cytoplasm and its inherent properties. Here, we performed Fluorescence Recovery After Photobleaching (FRAP) in tip-growing *Physcomitrella patens* cells, to determine the diffusion coefficient of 3xmEGFP, and calculate an effective cytoplasmic viscosity. In order to interpret the experimental measurements correctly and accurately estimate the diffusion coefficient, we developed a three-dimensional comprehensive computational model of the FRAP process, including particle diffusion, the cell boundary effects, and the optical properties of the scanning confocal microscope. To the best of our knowledge, this is the first time such an estimate of the viscosity for particles at this length scale is reported for a plant cell. Our model allows us to determine the degree at which cell boundary and optical effects confound the interpretation of FRAP recovery curves, the bound fraction of fluorescent proteins, and the number of dynamic states of a given fluorescent protein. The presented FRAP model has a wide range of applicability across many cell types including plant, animal, and fungal cells, particularly in the presence of otherwise prohibitive geometries.

1. Introduction

World crop demand is expected to grow by 48% by 2050 [1], therefore, building a mechanistic understanding of plant growth is crucial to provide the technology necessary to feed a growing world population. Because plant growth is dependent on specific patterns of cell growth and division, it is essential to fully understand these processes to be able to engineer plants with desirable morphological characteristics. The moss *Physcomitrella patens* is an ideal model organism to study plant cell growth; it has unparalleled genetics similar to yeast, with a well characterized genome sequence [2–5], and due to its size provides excellent imaging capabilities. Furthermore, this model plant is particularly relevant for studies of drought tolerance [6–9], and for bio-technological applications [8, 10–12]. Nevertheless, in order to develop a mechanistic and quantitative understanding of plant cell growth, it is important to characterize intracellular transport processes that facilitate growth in these cells.

Many cellular processes that are critical for growth, function and survival, including active transport of cellular cargo to the tips of growing cells, are dependent on the properties of the surrounding medium, i.e. the cytoplasm. While the cytoplasm of cells is a complex fluid comprised of proteins, cytoskeletal filaments, membranes, and other macromolecules, the cytoplasmic viscosity is typically defined as the viscosity experienced by small tracer particles such as GFP or fluorescent quantum dots introduced into cells [13, 14]. Cytoplasmic viscosity, hereafter the viscosity, is therefore a crucial parameter in modeling of

1

many transport processes in cells [15, 16]. However, geometric confinement and molecular crowding [17–21], hydrodynamic effects due to active transport [22], or cytoplasmic streaming in fast growing cells such as pollen tubes [23] make accurate measurements of viscosity challenging. The moss, while suffering from similar geometric and crowding effects, does not exhibit large organelle streaming [24], making it amenable for the use of optical techniques to measure diffusion of such small molecules, which would allow for an accurate estimate of the viscosity.

The most commonly used non-invasive, optical methods in literature for the measurement of molecular diffusion are single-particle tracking, Fluorescence Correlation Microscopy (FCS), and Fluorescence Recovery After Photobleaching (FRAP). When possible, single particle tracking gives excellent results, but this approach requires being able to image and track single fluorescently labeled targets in three dimensions, over the time scales relevant to the objects' motion [25]. FCS is an attractive alternative [17, 26], which does not use information at the single-particle level, however, it does require equipment capable of high temporal resolution.

FRAP [27, 28] provides another alternative to these approaches since it makes it possible to study diffusive behavior at long time (seconds) and length (microns) scales, and it has been extensively used to characterize diffusion of many different sizes of particles across different cell types, such as GFP in *E. coli* [29], GR-GFP in mouse adenocarcinoma cells [30], and others [31, 32]. Determining diffusion coefficients, and with that effective viscosity, from FRAP recovery curves has a series of challenges, however. In particular, the recoveries are affected by the presence of geometric boundaries, the shape and size of the Region of Interest (ROI) that is used, and features of the optical setup. Despite a large number of studies conducted with the aim of correctly interpreting FRAP recovery curves over the past three decades [28, 33–41], the authors are not aware, of any studies that correct for the three-dimensional nature of the FRAP ROI, imaging and bleaching effects, and the role of geometric boundaries in a systematic way, even though these have been noted as potential hazards in analysis [42]. Additionally, there are no simple analytical approaches for calculating the expected recovery in the vicinity of a complex boundary, such as the tip of a growing cell.

To measure diffusion of small molecules in growing moss cells, here, we conducted FRAP experiments for 3xmEGFP molecules, in conjunction with a comprehensive computational model of the entire FRAP process. Our coarse-grained three-dimensional approach incorporates fluctuating fluid behavior as well as the properties of the confocal system (imaging and bleaching), cell shape and ROI related effects, and is used to determine the diffusion coefficient, hence the viscosity, from experimental recovery data.

2. Materials and Methods

2.1 Cell Culture and Sample Preparation

In order to conduct FRAP experiments on *Physcomitrella patens*, microscope samples were prepared in QR-43C chambers (Warner Instruments) as follows. First, 25 mm bottom coverslips were plasma treated for three minutes to yield a hydrophilic surface. A solution of 0.8% type VII agarose in PpNO$_3$ medium (refer to Furt et al. 2013 [43] for details) was melted then added directly to the coverslips. Moss tissue was cultured for seven days after sub-culturing and on cellophane placed directly on top of the liquid phase agar. To obtain flat cultures, a second untreated coverslip was placed on top of the moss and flattened using a blunted syringe. Agarose was solidified by placing the cultures onto a surface at 12°C. Once the agarose solidified, the top coverslip was gently removed from the top of the preparation. The remaining preparation was submerged in PpNO$_3$ and the cellophane was removed. With the moss firmly adhered to the agarose, the entire coverslip was added to the QR chamber. The chambers were capped with 18 mm coverslips and connected to silicone tubing with a wall thickness of 0.018 in. The tubing was connected to a peristaltic pump and liquid PpNO$_3$ was perfused through the chambers over night. Liquid PpNO$_3$ was made two days prior to perfusion and was filter sterilized immediately before its use. During latrunculin B treatment, a solution of 5 μM or 10 μM latrunculin B was added in liquid PpNO$_3$ and perfused for 20 minutes as indicated.

2.2 Confocal Imaging

FRAP experiments were conducted using the Leica TCS SP5 scanning confocal microscope and the Leica FRAP Wizard. To conduct FRAP, a 63X objective was used with a numerical aperture (NA) of 1.4. In the software settings, the pinhole was set to 2.00 airy disks and the camera zoom was set to 9. Images of 256X256 pixels were acquired with a depth of 12bits. To visualize 3xmEGFP, the Argon laser was

set to 75% power with a bidirectional scanning speed of 2800 Hz and the 488 nm laser line was set to 10% power in the FRAP wizard. The emission bandwidth for 3xmEGFP was set between 499 nm and 546 nm. During bleaching events, all laser lines were set to 100%.

2.3 Experimental Measurement of Point Spread Function

In order to experimentally measure the Point Spread Function (PSF) of the confocal microscope, beads were used from the Ivitrogen PS-Speck Microscope Point Source Kit P7220 (Thermo Fisher Scientific, Waltham, MA). Preparations were made by adding 5 μL of 0.01% polylysine and 5 μL of bead solution to a dry microscope slide. A coverslip was then placed directly onto the slide and sealed with wax. Beads were visualized and measured with the Leica TCS SP5 scanning confocal microscope, using the settings described in **Section 2.1**. Green fluorescent beads were used to match the 3xmEGFP fluorophore, and z-stacks of the 175 nm beads were taken. From these z-stacks, a three-dimensional reconstruction of the bead's intensity profile was created as shown for the green beads in **Figure 2A**. These profiles were then used to determine the three dimensional parameters of the PSF.

To correct for the fact that the 175 nm beads were not an ideal point source, a three dimensional fitting routine was written. During this process, z-stacks for an ideal three dimensional 175 nm bead were generated. These bead image stacks were then convolved with the product of two three dimensional Gaussians from Eq. 11 with parameters w_0 and z_R. Theoretically generated and experimentally obtained PSFs are compared in **Figure 2A**. A sum of squared differences between the two PSFs was calculated and minimized to determine the parameters w_0 and z_R. A heat map showing the parameter range scanned illustrating the goodness of fit is given in **Figure S2** in the **Supporting Material**, and the parameters obtained are summarized in **Table SII** in the **Supporting Material**. These parameters were then used in the simulation of the excitation and emission schemes during confocal imaging.

2.4 Post Acquisition Processing

After capture, all FRAP images were subjected to an initial processing step to yield recovery curves. This procedure was chosen to resolve confounding factors that can influence the interpretation of FRAP results. Specifically, we examined confocal detector linearity (**Section S6**), image acquisition photobleaching (**Section S7**), and the effects of imaging and photobleaching away from the medial cell plane (**Section S8** in the **Supporting Material**). With this information we then constructed the FRAP processing scheme depicted in **Figure S4** in the **Supporting Material**. This flowchart illustrates how the experimental and simulated FRAP images were processed and analyzed to yield the data presented throughout the main text.

Experimental FRAP tiff stacks $I(x, y, t)_i$ were analyzed with an ImageJ macro. The subscript i represents the ith replicate tiff stack for a particular experimental condition. The macro was written to track the photobleached ROI throughout the fluorescence recovery. The macro conducted background subtraction and divided the ROI fluorescence intensities by the ROI prebleach intensity to yield $R_o^{\exp}(t)_i$ [39], namely,

$$R_o^{\exp}(t)_i = \frac{\langle I(x,y,t)_i\rangle_{(x,y)\in\text{ROI}} - \langle I(x,y,t)_i\rangle_{(x,y,t)\in\text{BackROI}}}{\langle I(x,y,t)_i\rangle_{(x,y)\in\text{ROI},t<0} - \langle I(x,y,t)_i\rangle_{(x,y,t)\in\text{BackROI}}} \quad . \tag{1}$$

Here $\langle ... \rangle$ denotes averaging about the corresponding subscripts inside the parenthesis, i.e.,

$$\langle ... \rangle_{(j)} = \frac{1}{n}\sum_{j=1}^{n} \quad . \tag{2}$$

The subscript ROI represents the photobleaching ROI and the subscript BackROI represents the background ROI. All subsequent FRAP recovery curve processing was then conducted on the time dependent curves $R_o^{\exp}(t)_i$. Simulated recovery curves were subjected to the same normalization without background subtraction to yield $R^{\sim}(t)_i$.

2.5 FRAP Parameter Minimization

To identify the simulation parameters best fitting the recovery curves produced by experiments, a least squares minimization routine was used. Initially, averaged experimental recovery curves $R^{\exp}(t)$ were

characterized into classes $R_T^{\exp}(t)$ and $R_S^{\exp}(t)$, depending on if they were produced from the tip or shank of the cell, respectively. Similarly, the averaged simulation recovery curves were characterized to produce $R_T^{\sim}(t)_{D,K,w_0}$ and $R_S^{\sim}(t)_{D,K,w_0}$. Here D is the diffusion coefficient, K is the bleaching proportionality coefficient, and w_0 is the bleaching probability beam waist used for the simulation. The best fit parameters for each experimental condition were found by minimizing the sum of squares differences between the experiment and simulation, for both the tip and shank, i.e.,

$$\arg\min_{w_0,D,K_t,K_s} \left[\sum_{t>0} (R_T^{\exp}(t) - R_T^{\sim}(t)_{D,K_t,w_0})^2 + \sum_{t>0} (R_S^{\exp}(t) - R_S^{\sim}(t)_{D,K_s,w_0})^2 \right] . \qquad (3)$$

These parameters were found by allowing the tip and shank to have the same diffusion coefficient D. The bleaching proportionality coefficient, K, was split into two independent parameters K_t and K_s, for the tip and shank, respectively, to improve the resultant fit. The difference between K_t and K_s indicates that some underlying physical process may be altering the initial bleach depths at the tip and shank (**Table SIV** in the **Supporting Material**). Understanding the cause of this difference is beyond the scope of this paper.

Determination of the errors associated with the parameters determined from the minimization procedure is described in **Section S10** in the **Supporting Material**.

2.6 Fourier Analysis of Spatial Recovery

Quantification of the directionality of fluorescence recovery was performed by subsampling the cropped ROIs into angular sectors about their centers. To reduce the noise associated with small regions of interest, a sliding window average was used. This sliding window was rotated 360 degrees and averaged about the horizontal axis of the ROI, producing an intensity profile that was dependent on the angular position of the sliding window, as shown in **Figure S12** in the **Supporting Material**. To investigate fundamental modes of spatial recovery, the angular intensity profiles were reconstructed using a Fourier cosine series [29], namely,

$$I_{\mathrm{v}}(\theta) = \sum_{n=0}^{\infty} f_n(\theta) = \frac{a_0}{2} + \sum_{n=1}^{\infty} a_n \cos(n\theta) \qquad (4)$$

with a_n denoting the amplitude of the nth Fourier mode.

2.7 GPU Accelerated Computation

Due to the large number of potential FRAP model parameters that needed to be scanned, we parallelized the simulation to take advantage of General Purpose Graphics Processing Unit (GPGPU) computing. We used the Single Instruction Multiple Thread (SIMT) parallelization model of NVidia's CUDA platform to make an accelerated parallel version of the software described here. By simultaneously simulating different a particle's motion in every thread on the GPU, simulation time was reduced approximately by a factor of 60, in addition to improvements in power and cost efficiencies by factors of two and three, respectively (see [44] for computational details).

3. FRAP Model

FRAP was originally, though under a different name, introduced by the work of Axelrod et al. [45], where a single Gaussian beam bleach was considered in two dimensions in an infinite domain. Without the consideration of a Point Spread Function (PSF), the analysis consisted of finding half-recovery times, and estimating diffusion coefficients from the size of the bleach spot. This approach was expanded on by Soumpasis and coauthors [27] by solving the full recovery profile for a two-dimensional sharp disk. Braga et al. [34] two decades later, provided an analytical solution, taking into account the PSF—though assuming it has a Gaussian profile in three dimensions—of the bleach in an infinitely large system without boundaries. Sprague and coauthors [35] present FRAP in the context of reaction-diffusion systems, and while their analysis involved a sharp disk ROI and no PSF, they discuss how multiple phases of recovery can be analyzed. More recently, Kang et al. in a series of papers [40, 46, 47] incorporated the finite-time of the bleaching process, and find this effect to be very strong (especially with multiple bleaches), stating

4

that it not be ignored. Nevertheless, as they worked to produce an analytical model, they had to disregard the imaging PSF, imaging time, and the presence of finite boundaries. Hallen and coauthors [38] took the reaction-diffusion model further, and produce an analytical equation for recovery given a conical disk photobleaching region, although as with many other analytical approaches, it is placed in an infinite domain.

The effect of boundaries during FRAP has been discussed by several groups as well. Mai et al. [33] used a two-dimensional particle-based method to examine the effects of reaction kinetics near boundaries, but instead of the actual PSF, they used a sharp bleach disk. Sbalzarini and coauthors [36] considered an arbitrary three-dimensional geometry, and also used a particle-based simulation. This is a scheme in which a single simulation is done for a set of baseline parameters, and from there, the resulting recovery curve is rescaled to fit the experimental data, and that rescaling can be used to calculate the diffusion coefficient. While a powerful technique, these approaches rely on the time-scale-invariance of the process, which is not true in the case where the bleaching and imaging times cannot be considered zero.

In their recent work, Fritzsche et al. [41] provided step-by-step instructions for producing and examining FRAP data, and suggest fitting the recovery curves to an increasing series of exponential fits—single, double, if necessary triple, etc. This series of fits allowed them to identify how many processes are occurring, and determine associated diffusion coefficients using the Axelrod method [45] of half-times. While the associated analysis uses the half-time approximation method here, it does not claim to be excessively accurate, and the authors additionally warned the readerr to make sure that they are performing FRAP a sufficient distance away from any boundaries in an isotropic region. This is important, because (as we demonstrate later), geometric effects are capable of making a double-exponential fit appropriate, despite the presence of a single actual diffusion coefficient.

In order to address the shortcomings of the earlier models, and accurately measure the diffusive dynamics of a given molecule in complex tip geometries, we created a rigorous, particle-based simulation that consists of non-interacting Brownian particles, with a constant diffusion coefficient [48]. As a first approximation, we moodeled the moss geometry as cylinder with a hemispherical cap (**Figure 1A**). The simulation also incorporates properties of the optical system, i.e. imaging and bleaching, finite scan rates of the confocal microscope, the Point Spread Function (PSF), and ROI size and shape related effects, as described below.

3.1 Diffusion of Fluorescent Particles

We used Brownian dynamics to simulate the diffusion of fluorescent particles in the moss geometry [49, 50]. The particles were assumed to be in a fluid with a very low Reynolds number, in which inertial effects are negligible, and the Stokes equation, i.e.,

$$\zeta \frac{d\vec{r}}{dt} = \vec{\xi}(t) \tag{5}$$

applies for each particle. Here $\xi_i(t)$ is the ith sample of random Gaussian noise with the properties

$$\langle \xi_i(t) \rangle = 0 \tag{6}$$
$$\langle \xi_i(t)\xi_j(t') \rangle = 2k_B T \zeta \delta_{ij} \delta(t - t') \ . \tag{7}$$

Assuming spherical particles with radius R, the friction coefficient, ζ, is given by

$$\zeta = 6\pi\eta R \tag{8}$$

for the dynamic viscosity η. We can relate this ζ to the diffusion coefficient D, using the Einstein relation

$$D = \frac{k_B T}{\zeta} \ . \tag{9}$$

The particles in the simulation were constrained to stay within the region inside a hemisphere-capped cylinder, as shown in **Figure S3A** in the **Supporting Material**. This shape was chosen to mimic the geometry of the tip of the moss caulonemal cell and correct for cell boundary affects during FRAP [33]. The constraint was imposed by adding an elastic collision between the particles and the boundary of the moss geometry, displayed in **Figure S3B** and **S3C**. For each particle, where v_i is the velocity before collision, during at each time step, a line segment is drawn from the previous position along its direction of travel. For each of the three boundary types (flat end, cylindrical sides, hemispherical tip), the next
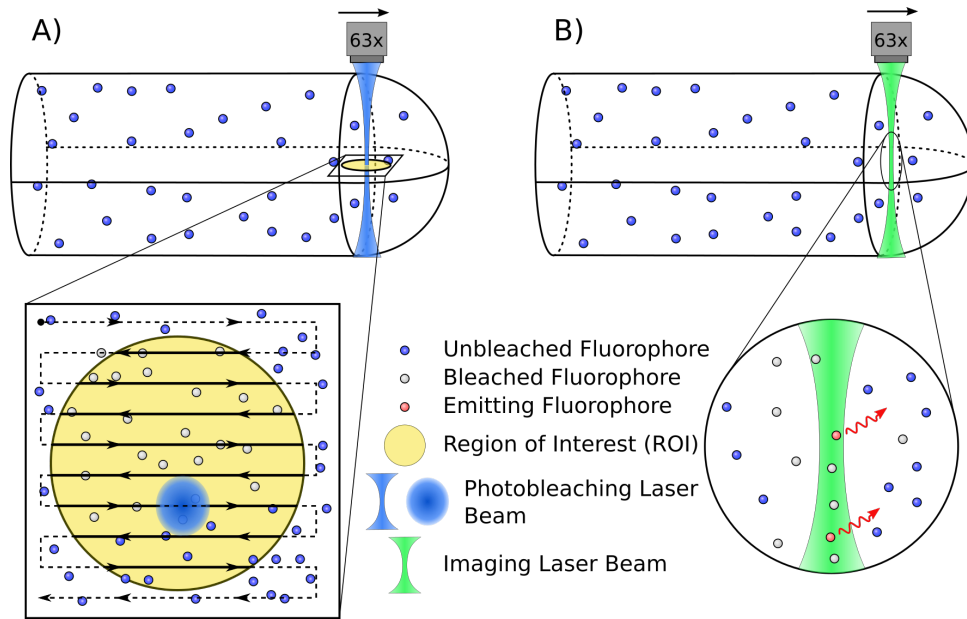
Figure 1. Illustration of 3D scanning confocal FRAP simulation. A) Scanning photobleach in confined finite particle simulation. Arrows indicate the bleaching pattern of the Gaussian photobleaching laser beam within the yellow circular region. B) Simulated particle excitation and emission. Here the green diffraction limited laser scans across the image and locally excites fluorophores that emit red light. In both figures A) and B) raster scanning happens at $1400Hz$. Images not to scale.

point is tested to check if it is out of bounds. If it is, the intersection between the line segment and the boundary is found. Out of these intersections, the first one reached is chosen as the collision to do. The position of the particle is set to this intersection point, and the amount of extra distance is recorded. The velocity vector is reflected along the surface normal $\hat{n}$, and the final velocity $\mathbf{v}_f$ is determined from the initial velocity $\mathbf{v}_i$ by

$$\mathbf{v}_f = \mathbf{v}_i - 2\hat{n}(\mathbf{v}_i \cdot \hat{n}) \ . \tag{10}$$

The particle then repeats the movement process (including additional collisions, if they happen) using the remaining amount of distance.

3.2 Confocal Imaging and Bleaching

To determine the parameters for this model, we first measured the Point Spread Function (PSF) of the microscope by imaging fluorescent beads [51]. For a point source located at the coordinates (x, y, z), the PSF in a confocal imaging system can be modeled by a Gaussian beam [52]. The Gaussian beam is of this form because it is the product of two three-dimensional excitation and emission Gaussians, as shown in **Figure S1B** in the **Supporting Material**. Both w_0 and z_R are experimentally determined from the PSF of the microscope as described in **Section 2.3** and **Figure 2** in the **Supporting Material**.

As the microscope rasters across the image, it illuminates an area, causing the fluorophores in that area to fluoresce. For the model, it is assumed that the intensity of the emission of an illuminated particle is directly proportional to the intensity of the excitation light it experiences. With all the nearby fluorophores emitting an amount of light, some of that light then travels back up the microscope objective, where it is focused into a light detector. This means that the intensity at a point $\mathbf{R}$ from a particle at point source at $\mathbf{P}_i$ is the product of the intensity the point experiences from the excitation beam ($\mathbf{I}_{ex}$) and the intensity the microscope reads from the point($\mathbf{I}_{em}$), i.e.

$$I(\mathbf{R}) = \sum_i I_{ex}(\mathbf{P}_i - \mathbf{R}) I_{em}(\mathbf{P}_i - \mathbf{R}) \ , \tag{11}$$

where I_{ex} and I_{em} represent the excitation and emission PSFs, respectively.

To analytically represent this process, we used a Gaussian approximation of the imaging system, I^{PSF} of the form

6

$$I^{\mathrm{PSF}}(x, y, z) = \frac{I_0}{w^2(z)} e^{-\frac{2(x^2 + y^2)}{w^2(z)}} \quad , \tag{12}$$

where the beam waist is given by

$$w(z) = w_0 \sqrt{1 + \frac{z^2}{z_R^2}} \quad . \tag{13}$$

Here, w_0 is the minimum beam waist and z_R is the Rayleigh range (see **Section 2.3** for details). After exploring this two dimensional parameter space, we were able to recapitulate the experimental three-dimensional diffraction limited laser beam with our Gaussian approximations as shown in **Figure 2A** and **Figure S2**.
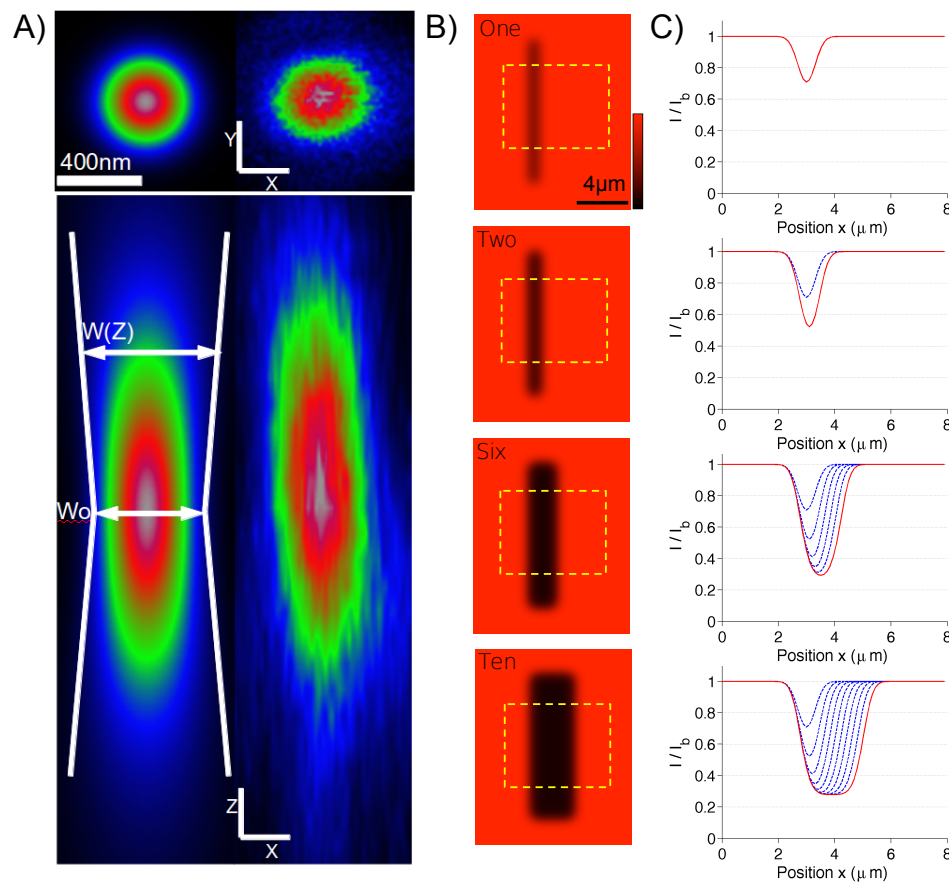

Figure 2. Point Spread Function (PSF). A) Gaussian approximation of the PSF, $I^{\mathrm{PSF}}(x, y, z)$, for 3xmEGFP (left) compared to the experimentally measured PSF for 175 nm bead (right). B) Example simulated rectangular photobleaching with one, two, and ten confocal laser scans using Eq. 14. Dashed yellow rectangles indicate regions in which horizontal lines scans were measured and averaged along their vertical axis. C) Horizontal line scans through simulated photobleaching images in (B) for one, two, six, and ten confocal laser scans. I represents fluorescence intensity and I_b represents mean simulated image background intensity. Red solid line indicates the final bleach result. Blue dashed lines indicate the bleach result following each successive laser scan.

With the imaging properties of the beam established, we then sought to determine its photobleaching properties. In order to simulate photobleaching, it was necessary to determine the spatial profile of an individual photobleaching event. This profile was characterized as a Gaussian beam, with a fluorophore-bleach probability ($P_{\mathrm{photobleach}}$) proportional to the beam intensity. As the microscope scans through a line at a speed much greater than diffusion (**Section S2** in the **Supporting Material**), we treated the photobleaching effect of a single horizontal line scan as a single instantaneous event. This was done by

convolving the Gaussian beam intensity against a boxcar function from $x = -a$ to $x = a$, i.e,

$$P_{\text{photobleach}}(x, y, z) = K \int_{-a}^{a} I(x + u, y, z) du = \int_{-a}^{a} \frac{K}{w^2(z)} e^{-\frac{2((x+u)^2 + y^2)}{w^2(z)}} du$$

$$= \frac{K}{w(z)} \left[\text{erf}\left(\frac{\sqrt{2}(x+a)}{w(z)} \right) - \text{erf}\left(\frac{\sqrt{2}(x-a)}{w(z)} \right) \right] \left[e^{-\frac{2y^2}{w^2(z)}} \right] \quad (14)$$

using the same $w(z)$ functional form as used for the imaging Gaussian, and using K as the bleaching proportionality coefficient. Simulated confocal scanning events using Eq. 14 are illustrated in **Figure 2B** and **2C**.
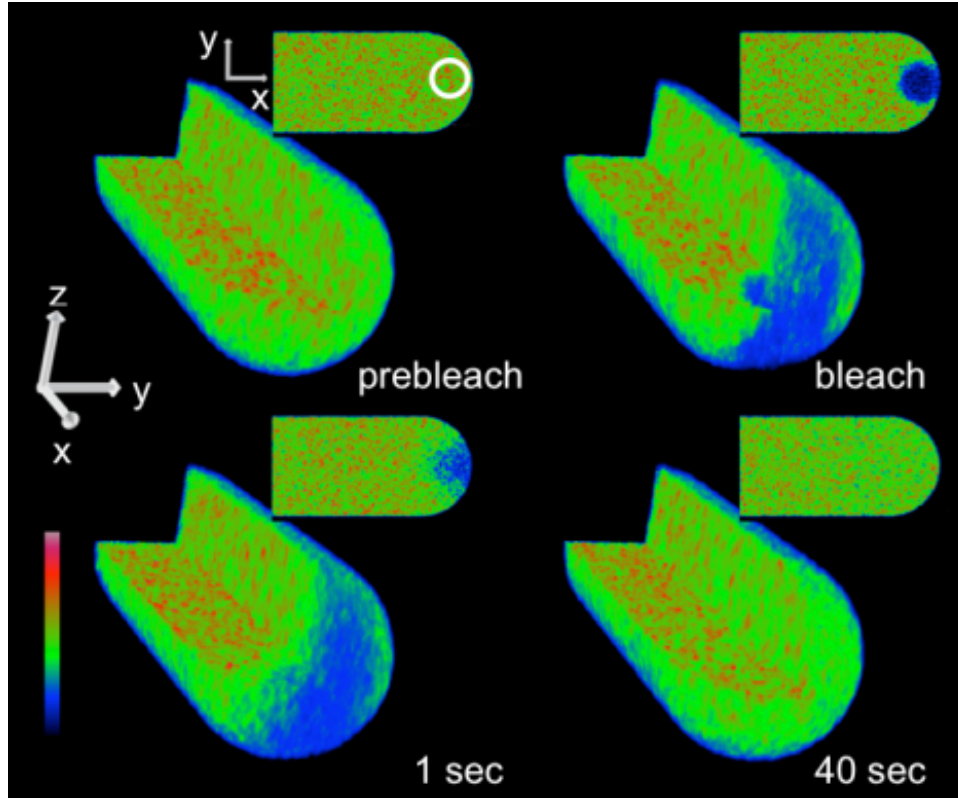
Figure 3. Three- and two-dimensional rendering of simulated scanning confocal photobleaching and recovery. Artificially fast imaging scan rates were used to illustrate three dimensional properties of the simulation.

The theoretical FRAP function resulted in a poor fit to the experimental FRAP profile when w_0 from the visualization Gaussian was used. To improve this fit, both the K and w_0 were used as open parameters in the fitting routine. The resulting w_0 was roughly two fold larger than the value obtained for imaging. The likely causes for this difference are light scattering at the high laser intensities used in bleaching, changes in refractive indices throughout the cell, and reactive oxygen species [53]. The theoretical estimations of K and w_0 were used as a starting point, and a range of parameters were scanned for both of them. The results from this minimization were used to measure diffusion, as explained in **Section 2.5**. A final snapshot from the simulations is depicted in **Figure 3**. The entire FRAP process is illustrated in **Sup Movie 1**, and **Sup Movie 2**.

4. Results

In order to better characterize the diffusion of proteins in plants cells, and measure the cytoplasmic viscosity, we conducted FRAP experiments on a cell line expressing three copies of unconjugated mEGFP in tandem (3xmEGFP). To improve the accuracy of our diffusion measurement we conducted photobleaching at two unique spatial locations within the cell. These locations include, the cell tip and a region distal

8

to the tip, referred to as the shank, as depicted in **Figure 4A**. We processed the curves to correct for acquisition photobleaching, and ensured that our experiments were in the linear range of the detector (**Sections 2.4** and **S6**). After processing, the tip and the shank regions exhibited a fast fluorescence recovery, on the order of a few seconds (**Figure 4B**). Additionally, recoveries at the cell tip exhibited a slower rate of recovery and higher fluorescence plateau when compared to the shank. To ensure that these recovery properties were not due to filamentous actin localization at the cell tip, we performed the same analysis in the presence of latrunculin B (**Figure 4C**). Latrunculin B treatment had no influence on the observed fluorescence recovery.

4.1 Cell Shape Influences Fluorescence Recovery

To determine that the differences observed at the tip and shank (**Figure 5A**) were a product of the cell boundary, and to measure the diffusion coefficient of 3xmEGFP, we simulated FRAP recovery curves at the tip and shank for a range of diffusion coefficients using the model described earlier. In our fitting routine (**Section 2.5**), we used one diffusion coefficient to fit both the tip and the shank, which yielded a diffusion coefficient of $D = 7.75 \pm 3.19 \ \mu m^2 s^{-1}$. The simulations at the cell tip exhibited both a slower rate of recovery and higher fluorescence plateau when compared to the shank, recapitulating experimental recoveries. The slower recovery at the cell tip is due to geometrical constraints provided by the apical plasma membrane, i.e., proteins cannot flow in or exchange in all directions as they can at the shank of the cell. The higher plateau at the cell tip is caused by photobleaching fewer particles at the cell tip since the three-dimensional Gaussian laser beam bleaches outside of the cell volume at the tip, in contrast to the fully encased beam at the cell shank. Our simulation results highlight the strong influence of boundaries on recovery, and shows that erroneous conclusions about the fraction of bound molecules and fluorescent mobility at the tip and shank can be made if such geometric effects are not taken into account.
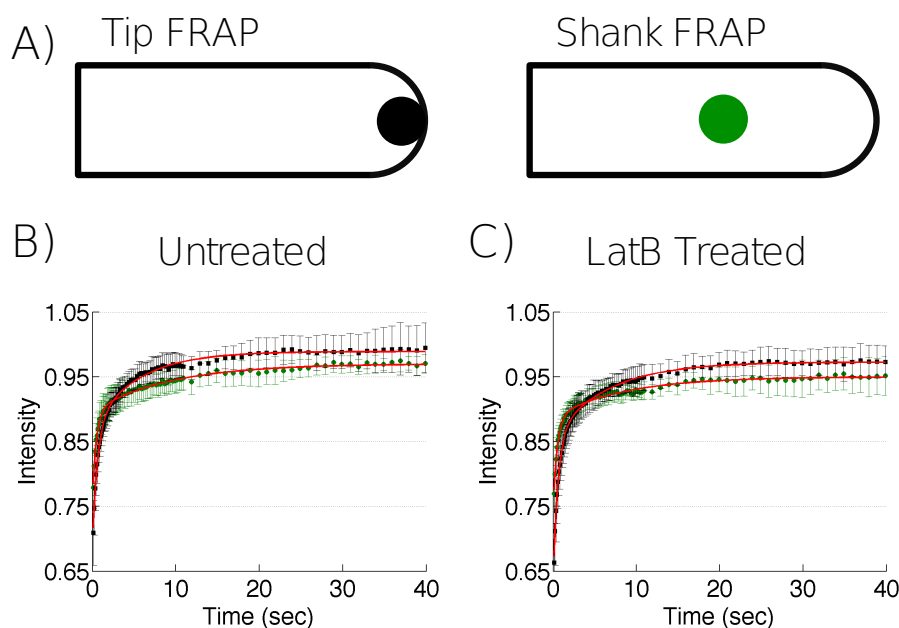
Figure 4. 3xmEGFP FRAP and curve fitting. A) Illustration of ROIs at the cell tip (black) and the cell shank (green). B) Fluorescence recovery at the tip (black) and shank (green) of cells expressing 3xmEGFP. C) Fluorescence recovery at the tip (black) and shank (green) of latrunculin B treated cell expressing 3xmEGFP. Red lines represent fits to a double exponential (Eq. 16).

4.2 Apparent Dynamic States of a Fluorophore

We found that cell shape can also influence the apparent number of dynamic states of a given fluorophore. By fitting our simulated recovery curves to a single and double exponential with GraphPad

9

| Model System and cell Type	Fluorescent Protein	Diffusion Coefficient $\mu m^2 s^{-1}$	MW kDa	Viscosity Relative to Water
Drosophila Embryo (FCS)[26]	Bcd-EGFP	7.4 ± 0.4	72	$7.3 - 8.1$
E. coli DH5 α (FRAP Fourier)[29]	GFP	7.7 ± 2.5	30	$7.5 - 14.6$
CHO-K1 (FRAP)[54]	GFP	27	30	2.8
Mouse Adenocarcinoma (FRAP)[30]	GR-GFP	3.4 ± 1.0	87	$12.1 - 22.2$
Swiss 3T3 (FRAP)[31]	BSA	6.8 ± 5.6	69	$4.6 - 48$
H1299 Cells (FRAP)[32]	P53-GFP	15.4 ± 5.6	70	$2.7 - 5.9$
P. patens Caulonema (FRAP)[this study]	3xmEGFP	7.75 ± 3.19	90	$4.8 - 11.6$

Table I. Diffusion coefficients across model systems.

Prism (GraphPad Software, La Jolla, CA), we found that, a double exponential model described our simulations better than the single exponential with a P-value less than 0.0001 (**Figure S10** and **Table SIII** in the **Supporting Material**). Without the prior knowledge that this is a result of the combination of geometric (cell shaper, ROI) and optical (imaging, bleaching) effects, one could incorrectly conclude that our simulation contains a fluorophore with two different diffusion coefficients. Since 3xmEGFP is supposed to be inert, this is further evidence that double exponential fitting does not reliably predict the number of dynamic states of a fluorophore. Our results suggest that extreme care should be exercised while fitting recovery curves with increasing series of exponential fits [41] in systems where boundary or optical effects can influence recovery, a point also raised by Fritzsche and co-workers [41].

4.3 Directional Recovery at the Cell Tip

To support our claim that cell shape can strongly influence the interpretation of FRAP curves and further validate our diffusion measurement, we examined the direction of fluorescence recovery by analyzing the spatial recoveries at the tip and shank (**Section S11** in the **Supporting Material**) as a function of time. To this aim, we cropped and averaged the photobleached regions (**Sup Movie 3** and **Figure 5B**). We could then detect intensity gradients as a function of angular position and time within the photobleached region (**Figures 5C and 5D**). The shape of these gradients at early time points demonstrates that the geometry at the cell tip limited the direction of fluorescence recovery. The same analysis at the cell shank yielded no observable gradient at early times (**Figure S15** in the **Supporting Material**). Additionally, the uniformity of fluorescence recovery at the cell shank indicates that hydrodynamics effects—such as those caused by cytoplasmic streaming—do not influence 3xmEGFP dynamics. This also indicates that the FRAP recovery at the extreme apex is affected by its position next to the apical plasma membrane, such that material can not flow in or exchange in all directions as it can with the FRAP region in the shank.

To quantitatively express the gradient's transition from the transient state (Δt_1) to the steady state (Δt_2), and to test the statistical significance of the difference between the observed gradients, we used a Fourier cosine series to express the angular intensity profile at the cell tip (**Section 2.6**). Over the time course of the fluorescence recovery, the coefficients of the first fundamental mode of the Fourier series, $a_1(t)$ decayed to zero (**Figure 5E**). At early times, Δt_1, the gradients exhibited time averaged Fourier coefficients significantly different than those observed during the steady state, Δt_2, (**Figure 5F**). This significant difference between the time averaged coefficients at Δt_1 and Δt_2 indicates that experimental noise artifacts did not produce the gradient observed at Δt_1, and is consistent with a cell boundary effect on diffusion. The simulations at the cell tip recapitulated the angular intensity profiles observed transiently ($\Delta t_1: 0-0.1s$) and at steady state ($\Delta t_2: 20-40s$) (**Figures 5B, 5E, 5F**, **S16** and **Sup Movie 3**). This agreement between the simulated and experimental recovery supports the accuracy of our measurement of 3xmEGFP diffusion and illustrates how cell shape can confound the interpretation of FRAP curves.
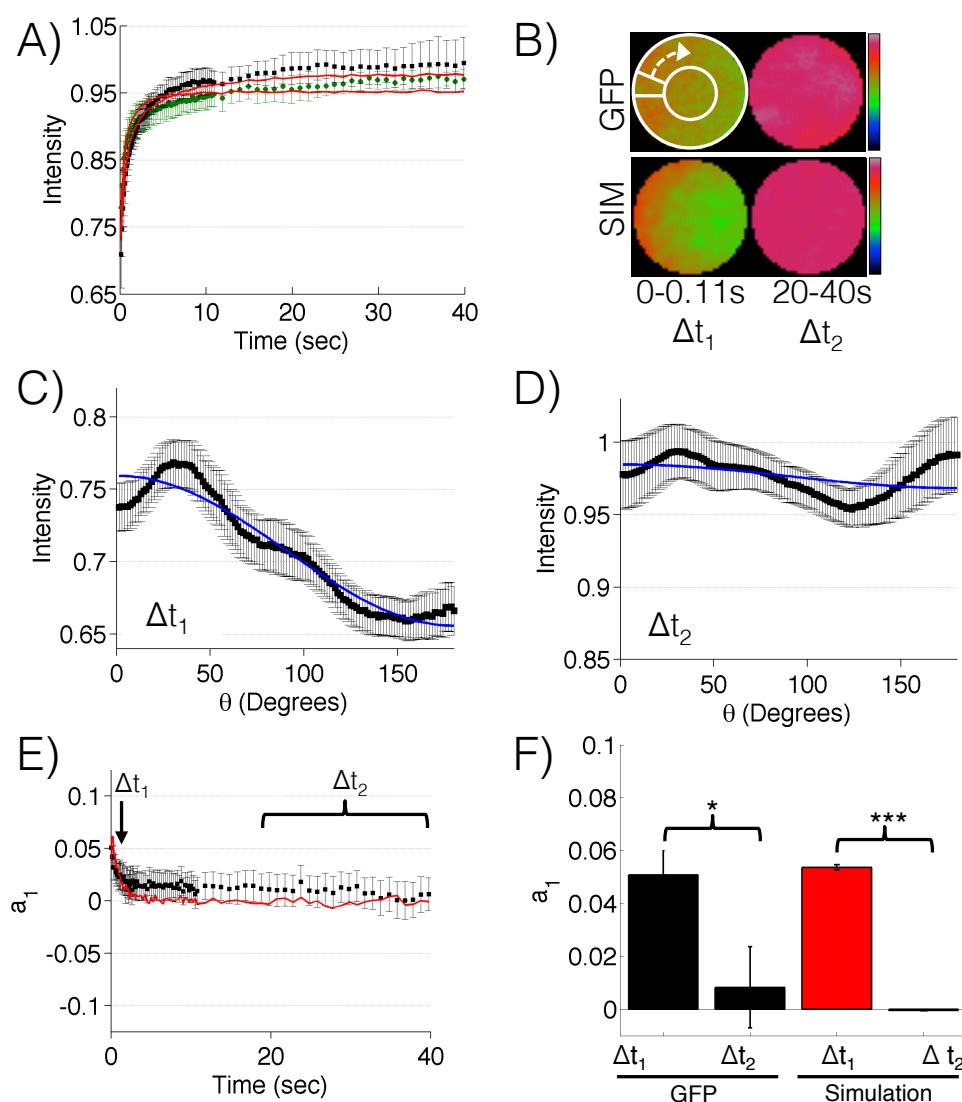
Figure 5. 3xmEGFP dynamics. A)Fluorescence recovery of 3xmEGFP cells at the tip (black squares) and shank (green circles). Best fit simulation indicated in red. $n = 14$ and 7 for the tip and shank, respectively. Error bars represent standard deviation. B) Cropped and frame averaged photobleaching ROI at the cell tip of 3xmEGFP cell line (top) and simulation (bottom). Time intervals for frame averaging are $\Delta t_1 = 0 - 0.11s$ and $\Delta t_2 = 20 - 40s$. $n = 14$ and 50, respectively. ROI is 4 μm in diameter with angular intensity profile window indicated. Image intensity denoted with rainbow lookup table. C-D) Angular intensity profile of 3xmEGFP at the cell tip during the time intervals Δt_1 and Δt_2. $\Delta t_1 = 0 - 0.11s$ (C) and $\Delta t_2 = 20 - 40s$ (D). First mode of the Fourier series, f_1, is indicated in blue. $n = 14$, error bars indicate standard error. E) Coefficients of the first mode of Fourier series, a_1, across time for 3xmEGFP (black) and simulation (red) for angular intensity profiles at the cell tip. $n = 14$ and 50 respectively; error bars indicate standard error. $\Delta t_1 = 0.11s$; $\Delta t_2 = 20 - 40s$. F) Fourier coefficients, a_1, for frame averaged angular intensity profiles. 3xmEGFP cells are indicated in black and the simulations are indicated in red. Differences between Δt_1 and Δt_2 for simulation and 3xmEGFP are significant with, $P < 0.05$ and $P < 0.001$ respectively. $n = 14$ and 50 respectively, error bars indicate standard error. $\Delta t_1 = 0 - 0.11s$; $\Delta t_2 = 20 - 40s$.

11

5.   Discussion

In this work we have characterized diffusion of 3xmEFGP molecules within the moss cytoplasm by conducting experimental and simulated FRAP. Our simulation incorporates the diffusing fluorescent particles under observation, the geometry of the cell tip, their appearance due to the three dimensional point spread function of the microscope, the experimentally measured bleaching probabilities, and the finite scan rate of the confocal microscope. Together, our experiments and simulations showed that the cell boundary and confocal imaging properties influenced the behavior of fluorescence recovery. Specifically, these effects influence the residence time of diffusing particles at the cell tip and the number of bleached fluorescent molecules, leading to erroneous measurements of diffusion coefficients, particle binding fractions, and the number of dynamics states of a particle when fit to simple FRAP models [27, 41, 55]. We also examined additional confounding factors such as detector linearity, and imaging and photobleaching in different cell planes. Although these factors did not influence our results, it is important to note that they could potentially confound FRAP analysis under different experimental conditions. Our simulation can be extended to other species and microscope setups, where the characteristics of the system make conventional analysis—such as the presence of complex boundaries—via analytical formulas impractical or impossible. For instance, our approach can be used in animals cells with protrusions complicating the FRAP regions, or with molecules diffusing on a nuclear membrane. This is particularly relevant as the FRAP model presented here is applicable to systems where the combined effects of the point spread function and scanning speed on fluoresce recovery are comparable to the diffusion rate of the fluorescent marker.

With our validated measurement of the 3xmEGFP diffusion coefficient, we can calculate the effective cytoplasmic viscosity of the moss cell for proteins of this size. We do this by estimating the radius, r, of the GFP protein from its molecular weight, and then using the Stokes-Einstein relation, $D = k_B T / 6\pi\eta r$, where $k_B T$ is Boltzmann constant times temperature, η is viscosity. Our calculated moss viscosity (shown in **Table I**) is consistent with measurements of cytoplasmic viscosity in other species. To the best of our knowledge, this is the first time measurement of a diffusion coefficient or cytoplasmic viscosity for proteins of this size in plants, which is particularly relevant since previous studies of diffusion in plants focused only on small molecules [56, 57]. Such measurements are important because they provide insight into all facets of cellular dynamics, which influence fundamental cellular processes such as growth, division, and cell signaling. Additionally, this viscosity measurement can be used to estimate diffusion of other species, as well as be incorporated into other mechanistic models of cellular growth.

Author Contributions

JK developed the simulations and JB performed the experiments. JK and JB analyzed data and wrote the manuscript. ZC and XH contributed to the development of GPU implementation of the simulations. ET and LV designed the research and wrote the manuscript.

Acknowledgments

Supporting Citations

References [58–60] appear in the **Supporting Material**.

References

1. Alexandratos, N., J. Bruinsma, et al., 2012. World agriculture towards 2030/2050: the 2012 revision. Technical report, ESA Working paper.

2. Vidali, L., and M. Bezanilla, 2012. *Physcomitrella patens*: a model for tip cell growth and differentiation. Current opinion in plant biology 15:625–631.

3. Vidali, L., R. C. Augustine, S. N. Fay, P. Franco, K. A. Pattavina, and M. Bezanilla, 2009. Rapid screening for temperature-sensitive alleles in plants. Plant physiology 151:506–514.

4. Rensing, S. A., D. Lang, A. D. Zimmer, A. Terry, A. Salamov, H. Shapiro, T. Nishiyama, P.-F. Perroud, E. A. Lindquist, Y. Kamisugi, et al., 2008. The *Physcomitrella* genome reveals evolutionary insights into the conquest of land by plants. Science 319:64–69.

5. Schaefer, D. G., and J.-P. Zrÿd, 1997. Efficient gene targeting in the moss *Physcomitrella patens*. The Plant J. 11:1195–1206.

6. Frank, W., D. Ratnadewi, and R. Reski, 2005. *Physcomitrella patens* is highly tolerant against drought, salt and osmotic stress. Planta 220:384–94.

7. Hirayama, T., and K. Shinozaki, 2010. Research on plant abiotic stress responses in the post-genome era: past, present and future. The Plant journal : for cell and molecular biology 61:1041–52.

8. Hohe, A., and R. Reski, 2005. From axenic spore germination to molecular farming. one century of bryophyte in vitro culture. Plant cell reports 23:513–21.

9. Proctor, M. C. F., M. J. Oliver, A. J. Wood, P. Alpert, L. R. Stark, N. L. Cleavitt, and B. D. Mishler, 2007. Desiccation-tolerance in bryophytes: a review. The Bryologist 110:595–621.

10. Gitzinger, M., J. Parsons, R. Reski, and M. Fussenegger, 2009. Functional cross-kingdom conservation of mammalian and moss (*Physcomitrella patens*) transcription, translation and secretion machineries. Plant biotechnology journal 7:73–86.

11. Roberts, A. W., and J. T. Bushoven, 2007. The cellulose synthase (CESA) gene superfamily of the moss *Physcomitrella patens*. Plant molecular biology 63:207–19.

12. Saidi, Y., A. Finka, M. Chakhporanian, J.-P. Zrÿd, D. G. Schaefer, and P. Goloubinoff, 2005. Controlled expression of recombinant proteins in *Physcomitrella patens* by a conditional heat-shock promoter: a tool for plant research and biotechnology. Plant molecular biology 59:697–711.

13. Dijksterhuis, J., J. Nijsse, F. A. Hoekstra, and E. A. Golovina, 2007. High viscosity and anisotropy characterize the cytoplasm of fungal dormant stress-resistant spores. Eukaryotic cell 6:157–70.

14. Hayashi, K., C. G. Pack, M. K. Sato, K. Mouri, K. Kaizu, K. Takahashi, and Y. Okada, 2013. Viscosity and drag force involved in organelle transport: investigation of the fluctuation dissipation theorem. The European physical journal. E, Soft matter 36:136.

15. Howard, J., et al., 2001. Mechanics of motor proteins and the cytoskeleton. Sinauer Associates Sunderland, MA.

16. Phillips, R., J. Kondev, J. Theriot, and H. Garcia, 2012. Physical biology of the cell. Garland Science.

17. Weiss, M., M. Elsner, F. Kartberg, and T. Nilsson, 2004. Anomalous subdiffusion is a measure for cytoplasmic crowding in living cells. Biophysical journal 87:3518–24.

18. Banks, D. S., and C. Fradin, 2005. Anomalous diffusion of proteins due to molecular crowding. Biophysical journal 89:2960–71.

19. Luby-Phelps, K., P. E. Castle, D. L. Taylor, and F. Lanni, 1987. Hindered diffusion of inert tracer particles in the cytoplasm of mouse 3T3 cells. Proceedings of the National Academy of Sciences 84:4910–4913.

20. Seksek, O., J. Biwersi, and A. Verkman, 1997. Translational diffusion of macromolecule-sized solutes in cytoplasm and nucleus. The J. Cell Biol. 138:131–142.

21. Arrio-Dupont, M., G. Foucault, M. Vacher, P. F. Devaux, and S. Cribier, 2000. Translational diffusion of globular proteins in the cytoplasm of cultured muscle cells. Biophysical journal 78:901–7.

22. Houtman, D., I. Pagonabarraga, C. P. Lowe, A. Esseling-Ozdoba, A. M. C. Emons, and E. Eiser, 2007. Hydrodynamic flow caused by active transport along cytoskeletal elements. Europhys. Lett. 78:18001.

23. Kroeger, J. H., F. B. Daher, M. Grant, and A. Gieitmann, 2009. Microfilament orientation constrains vesicle flow and spatial distribution in growing pollen tubes. Biophys. J. 97:1822–1831.

24. Furt, F., K. Lemoi, E. Tüzel, and L. Vidali, 2012. Quantitative analysis of organelle distribution and dynamics in *Physcomitrella patens* protonemal cells. BMC Plant Biol. 12:70.

25. Qian, H., M. P. Sheetz, and E. L. Elson, 1991. Single particle tracking. analysis of diffusion and flow in two-dimensional systems. Biophysical journal 60:910.

26. Abu-Arish, A., A. Porcher, A. Czerwonka, N. Dostatni, and C. Fradin, 2010. High mobility of bicoid captured by fluorescence correlation spectroscopy: implication for the rapid establishment of its gradient. Biophys. J. 99:L33–L35.

27. Soumpasis, D., 1983. Theoretical analysis of fluorescence photobleaching recovery experiments. Biophys. J. 41:95–97.

28. Bajanca, F., V. Gonzalez-Perez, S. J. Gillespie, C. Beley, L. Garcia, E. Theveneau, R. P. Sear, and S. M. Hughes, 2015. In vivo dynamics of skeletal muscle dystrophin in zebrafish embryos revealed by improved FRAP analysis. eLife 4:e06541.

29. Elowitz, M. B., M. G. Surette, P. E. Wolf, J. B. Stock, and S. Leibler, 1999. Protein mobility in the cytoplasm

of *Escherichia coli.* J. Bacteriol. 181:197–203.

30. Stasevich, T. J., F. Mueller, A. Michelman-Ribeiro, T. Rosales, J. R. Knutson, and J. G. McNally, 2010. Cross-validating FRAP and FCS to quantify the impact of photobleaching on in vivo binding estimates. Biophys. J. 99:3093–101.

31. Luby-Phelps, K., F. Lanni, and D. L. Taylor, 1985. Behavior of a fluorescent analog of calmodulin in living 3t3 cells. J. Cell Biol. 101:1245–1256.

32. Hinow, P., C. E. Rogers, C. E. Barbieri, J. A. Pietenpol, A. K. Kenworthy, and E. DiBenedetto, 2006. The DNA binding activity of p53 displays reaction-diffusion kinetics. Biophys. J. 91:330–42.

33. Mai, J., S. Trump, I. Lehmann, and S. Attinger, 2013. Parameter importance in FRAP acquisition and analysis: a simulation approach. Biophys. J. 104:2089–2097.

34. Braga, J., J. M. Desterro, and M. Carmo-Fonseca, 2004. Intracellular macromolecular mobility measured by fluorescence recovery after photobleaching with confocal laser scanning microscopes. Mol. Biol. Cell 15:4749–60.

35. Sprague, B. L., and J. G. McNally, 2005. FRAP analysis of binding: proper and fitting. Trends Cell Biol. 15:84–91.

36. Sbalzarini, I. F., A. Mezzacasa, A. Helenius, and P. Koumoutsakos, 2005. Effects of organelle shape on fluorescence recovery after photobleaching. Biophys. J. 89:1482–1492.

37. Pucadyil, T. J., and A. Chattopadhyay, 2006. Confocal fluorescence recovery after photobleaching of green fluorescent protein in solution. J. Fluoresc. 16:87–94.

38. Hallen, M. A., and A. T. Layton, 2010. Expanding the scope of quantitative FRAP analysis. J. Theor. Biol. 262:295–305.

39. McNally, J. G., 2008. Quantitative FRAP in analysis of molecular binding dynamics in vivo. Methods Cell Biol. 85:329–51.

40. Kang, M. C., C. A. Day, E. DiBenedetto, and A. K. Kenworthy, 2010. A quantitative approach to analyze binding diffusion kinetics by confocal FRAP. Biophys. J. 99:2737–2747.

41. Fritzsche, M., and G. Charras, 2015. Dissecting protein reaction dynamics in living cells by fluorescence recovery after photobleaching. Nat. Protoc. 10:660–680.

42. Lorén, N., J. Hagman, J. K. Jonasson, H. Deschout, D. Bernin, F. Cella-Zanacchi, A. Diaspro, J. G. McNally, M. Ameloot, N. Smisdom, M. Nydén, A.-M. Hermansson, M. Rudemo, and K. Braeckmans, 2015. Fluorescence recovery after photobleaching in material and life sciences: putting theory into practice. Q. Rev. Biophys. 48:323–387.

43. Furt, F., Y. C. Liu, J. P. Bibeau, E. Tüzel, and L. Vidali, 2013. Apical myosin XI anticipates f-actin during polarized growth of *Physcomitrella patens cells.* Plant J. 73:417–428.

44. Kingsley, J., Z. Chen, J. Bibeau, L. Vidali, X. Huang, and E. Tüzel, 2014. A GPU accelerated virtual scanning confocal microscope. In High Performance Extreme Computing Conference (HPEC), 2014 IEEE, 1–6. IEEE.

45. Axelrod, D., D. E. Koppel, J. Schlessinger, E. Elson, and W. W. Webb, 1976. Mobility measurement by analysis of fluorescence photobleaching recovery kinetics. Biophysical journal 16:1055–69.

46. Kang, M., C. A. Day, K. Drake, A. K. Kenworthy, and E. DiBenedetto, 2009. A generalization of theory for two-dimensional fluorescence recovery after photobleaching applicable to confocal laser scanning microscopes. Biophysical journal 97:1501–11.

47. Kang, M., C. A. Day, A. K. Kenworthy, and E. DiBenedetto, 2012. Simplified equation to extract diffusion coefficients from confocal FRAP data. Traffic (Copenhagen, Denmark) 13:1589–600.

48. Mogilner, A., and D. Odde, 2011. Modeling cellular processes in 3d. Trends in cell biology 21:692–700.

49. Öttinger, H. C., 1996. Stochastic processes in polymeric fluids: tools and examples for developing simulation algorithms. Springer, Berlin; New York.

50. Arpağ, G., S. Shastry, W. O. Hancock, and E. Tüzel, 2014. Transport by populations of fast and slow kinesins uncovers novel family-dependent motor characteristics important for in vivo function. Biophys. J. 107:1896–904.

51. Cole, R. W., T. Jinadasa, and C. M. Brown, 2011. Measuring and interpreting point spread functions to determine confocal microscope resolution and ensure quality control. Nat. Protoc. 6:1929–1941.

52. Qian, H., and E. L. Elson, 1991. Analysis of confocal laser-microscope optics for 3-d fluorescence correlation spectroscopy. Applied optics 30:1185–1195.

53. Zheng, Q., S. Jockusch, Z. Zhou, and S. C. Blanchard, 2014. The contribution of reactive oxygen species to the photobleaching of organic fluorophores. Photochem. Photobiol. 90:448–454.

54. Swaminathan, R., C. P. Hoang, and A. S. Verkman, 1997. Photobleaching recovery and anisotropy decay of green fluorescent protein GFP-S65T in solution and cells: Cytoplasmic viscosity probed by green fluorescent protein translational and rotational diffusion. Biophys. J. 72:1900–1907.

55. Motulsky, H., and A. Christopoulos, 2004. Fitting models to biological data using linear and nonlinear regression : a practical guide to curve fitting. Oxford University Press, Oxford ; New York.

56. Rutschow, H. L., T. I. Baskin, and E. M. Kramer, 2014. The carrier AUXIN RESISTANT (AUX1) dominates auxin flux into *Arabidopsis* porotoplasts. New Phytol. 204:536–544.

57. Rutschow, H. L., T. I. Baskin, and E. M. Kramer, 2011. Regulation of solute flux through plasmodesmata

in the root meristem. Plant Physiol. 155:1817–1826.

58. Waters, J. C., 2009. Accuracy and precision in quantitative fluorescence microscopy. J. Cell Biol. 185:1135–1148.

59. Phair, R. D., S. A. Gorski, and T. Misteli, 2004. Measurement of dynamic protein binding to chromatin in vivo, using photobleaching microscopy. Methods Enzymol. 375:393–414.

60. Dalal, R. B., M. A. Digman, A. F. Horwitz, V. Vetri, and E. Gratton, 2008. Determination of particle number and brightness using a laser scanning confocal microscope operating in the analog mode. Microsc. Res. Tech. 71:69–81.